Subsurface Planetary Drilling Fault and Anomaly Detection

Sarah Boelter[1], Greta Brown[1], Rene Mai[2], Ebasa Temesgen[1], Lucas Weber[3], Thomas Stucky[4], Brian Glass[5], Maria Gini[1]

***Abstract*— In extraterrestrial planetary environments, environmental, computing, energy, and operational constraints require robotic agents to complete tasks without human supervision. Specialized extraterrestrial robotic drilling agents currently lack autonomous drilling capabilities, primarily because research into subsurface environment representation for autonomous drilling remains in its early stages. We validate work using online model-free time-series subspace analysis methods for noisy and sparse data to estimate drilling faults from drill avionics telemetry in Haughton Crater in the Canadian High Arctic. We also introduce a multivariate subsurface anomaly detection method that leverages sensor fusion of avionics telemetry evaluated on planetary analogs in Antarctica.**

I. Introduction

This paper focuses on "The Regolith and Ice Drill for Exploring New Terrain" (TRIDENT) [1], shown in Figure 1. The drill is a 1-meter rotary percussive drill manufactured by Honeybee Robotics and set as a payload for NASA's 2027 VIPER mission. The NASA Ames DIG Group has concentrated on advancing autonomy for the drilling system, with focus on subsurface state fault and anomaly detection and autonomous drilling capabilities [2]. Faults and anomalies are relatively rare, leading to sparse drilling fault data. TRIDENT gives indicators of drilling faults via telemetry, but lack of data makes training conventional machine learning models difficult. This work highlights and builds upon previous subspace-based change point detection techniques [2] for subsurface fault and anomaly detection. The major contributions are:

- Evaluation of our univariate subsurface fault and anomaly detection method, Enhanced Singular Spectrum Transformation (ESST) in a Mars analog [3] at Haughton Crater in the Canadian High Arctic.
- A novel method for multivariate fault and anomaly detection, Multivariate Enhanced Singular Spectrum Transformation (MESST), for sensor fusion of TRIDENT drill telemetry for signal stability and noise control, evaluated at planetary analogs [4], [5] at Schirmacher Oasis and Lake Untersee in Antarctica.

[1]University of Minnesota Twin-Cities, Minneapolis, USA {boelt072, brow6802,temes021 gini}@umn.edu
[2]Rensselaer Polytechnic Institute, Troy, USA {mair}@rpi.edu
[3]Friedrich-Alexander-Universität Erlangen-Nürnberg, Germany {lucas.weber}@fau.de
[4]KBR Wyle Serives LLC, Moffett Field, USA {thomas.stucky}@nasa.gov
[5]NASA Ames Research Center, Moffett Field, USA {brian.glass}@nasa.gov

Fig. 1. TRIDENT Drill at Lake Untersee for field testing in Antarctica January 2026

II. Related Work

A. Autonomy in Extraterrestrial Subsurface Environments

Extra-terrestrial autonomy remains limited. The 1997 Sojourner mission depended on Earth-based control, highlighting the need for onboard autonomy [6]. Earlier missions like Luna 16, 20, and 24 enabled deep drilling through heavy landers, unlike modern ∼200 kg rovers [7], motivating lightweight drilling research. The Scarab rover, developed by Carnegie Mellon's Field Robotics Center, focused on design and mobility without autonomy [8], while the Zoë rover demonstrated autonomous traversal and sampling in Mars-analog terrain [9]. Other efforts include burrowing robots [10], the Lunar Leaper [11], and the snake-like EELS system for subsurface exploration [12].

B. Timeseries Subspace Tracking

Subspace tracking maintains a low-dimensional representation of streaming data to detect system changes effectively for time-embedded, noisy, or incomplete signals [13]. Common methods include GROUSE [14] and PETRELS [15], with PETRELS offering faster, more robust convergence at higher computational cost. Subspace-based change-point detection (CPD) captures abrupt structural changes without

long histories by emphasizing signal shape and suppressing noise via decomposition. These methods use singular value decomposition ("SVD") on trajectory matrices to extract features around time t [16], [17], with Singular Spectrum Transformation (SST) comparing across time points to detect changes [16], [18].

C. Sensor Fusion in Signal Processing/Robotics

Sensor fusion combines data from multiple sensors to improve state estimation, with performance shaped by sensor count, data volume, and computational limits. It is used in applications such as power plants [19], welding defect detection [20], and robot localization [21], as well as for denoising and feature extraction [22]. Hankel matrix SVD, a discrete approximation of space-time POD [23], is widely applied in tasks such as seismic data reconstruction [24], fault detection in mechanical systems [25], structural identification [26], and rotating machinery diagnostics [27].

III. Methods

A. Subsurface Fault and Anomaly Detection

Enhanced Singular Spectrum Transformation (ESST) has shown strong performance in univariate drill fault and anomaly detection [28], [2]. Multivariate Enhanced Singular Spectrum Transformation (MESST) extends ESST to the multivariate case using a block Hankel matrix, enabling sensor fusion. MESST reduces change score noise and produces clearer fault and anomaly signals than ESST.

1) ESST: Subspace-based CPD methods use the singular value decomposition of of two Hankel matrices H_i and H_j with $i < t < j$ to extract representative sequences before and after $(+\delta t)$ some point in time t and compare them to provide a change point score [16], [17]. ESST has been demonstrated to outperform SST and other methods for the noisy signals encountered for robotic drills [2].

ESST embeds past and future subsequences into a single Hankel matrix and extracts a score by identifying characteristics. This incorporates future information into the final change score. We analyze the k-major right singular vectors V_k of the two-sided Hankel matrix, where the first half of columns are subsequences from time t and the second half from around $t + \delta t$:

$$\tilde{S}_T^t = \frac{\sum_{i=0}^{k-1} \sigma_i \left| \frac{1}{N} \left(\sum_{j=0}^{n/2-1} V^{i,j} - \sum_{j=n/2}^{n-1} V^{i,j} \right) \right|}{\sum_{i=0}^{k-1} \sigma_i}. \quad (1)$$

Using more characteristics yields a more complete representation of the time series. Accordingly, the improved change score is computed from multiple vectors of both Hankel matrices. The ESST algorithm enables this by modifying the Hankel matrix construction and utilizing the previously unused right singular vectors $V_{t,k}$. The ESST method parameters include rank k of the subspace, the number of sequences n, and the length w of the subsequences that make up the Hankel matrices, which are δt apart. For both the Haughton Crater and Antarctic field exercises, we fixed $\delta t = w/3$ to a third of the window size. From previous work, we found $k = 5$, $w = 70$ works for accurate online fault and anomaly detection with a telemetry sample rate of 40Hz.

2) MESST: Hankel matrices applied to time-series data contain the time history of data, with ascending skew-diagonal entries identical [23]. Hankel matrices have been used successfully with ESST [2]. Suppose a sensor produces a univariate stream of timeseries measurements $a(t)$, such that the stream of measurements is $a(t) = \begin{bmatrix} a(1) & a(2) & \dots & a(n+p-1) \end{bmatrix}^T$. The resulting univariate Hankel matrix formed from this sensor is thus

$$\mathbf{H}(a(t)) = \begin{bmatrix} a(t) & a(t-1) & \dots & a(t-n) \\ a(t-1) & a(t-2) & \dots & a(t-n-1) \\ \vdots & \vdots & \ddots & \vdots \\ a(t-p) & a(t–p–1) & \dots & a(t–n–p–1) \end{bmatrix}. \quad (2)$$

If $n = p$, the Hankel matrix will be square and thus symmetric, although that is generally not required. If multiple sensors provide separate univariate time series measurements of a process, it can be advantageous to combine them into a multivariate Hankel matrix. Let timeseries multivariate vector $\vec{q}(t)$ represent the measurements from k sensors at time t, such that $\vec{q}(t) = \begin{bmatrix} q_1(t) & q_2(t) & \dots & q_k(t) \end{bmatrix}$. A block Hankel matrix $\mathbf{H}(\vec{q}(t))$ can formed from the entries of $\vec{q}(t)$ as

$$\mathbf{H}(\vec{q}(t)) = \begin{bmatrix} \vec{q}(t) & \vec{q}(t-1) & \dots & \vec{q}(t-n) \\ \vec{q}(t-1) & \vec{q}(t-2) & \dots & \vec{q}(t-n-1) \\ \vdots & \vdots & \ddots & \vdots \\ \vec{q}(t-p) & \vec{q}(t–p–1) & \dots & \vec{q}(t–n–p–1) \end{bmatrix}. \quad (3)$$

Using the block Hankel matrix instead of the univariate matrix allows the use of techniques leveraging the relationship between different related sensors. For MESST, sensor fusion is achieved via a block Hankel matrix [23] constructed by:

$$\mathbf{H}_{ij} = \left[\mathbf{H}(\vec{q}(i)); |; \mathbf{H}(\vec{q}(j)) \right], \quad i < t < j, \quad (4)$$

embedding past and future subsequences. Taking its SVD,

$$\mathbf{H}_{ij} = \mathbf{U} \mathbf{\Sigma} \mathbf{V}^{i,j}, \quad (5)$$

we use the k-dominant right singular vectors $\mathbf{V}_k$ in equation (1) to compute a change score that highlights multivariate differences while reducing noise.

B. Methods of Evaluation

Evaluation of CPD and subspace distance metric algorithms is highly application-dependent, and while benchmarks [29] provide comparative frameworks, they may not fully capture noisy real-world sensor data. We evaluate ESST and MESST based on the specific constraints of our application.

1) F1 Score: Fault rarity limits the options for evaluating the effectiveness of ESST. CPD is often framed as a binary classification task: change or no change [30], [29], [31]. While prior work evaluates change points, we assess performance per sample, resulting in a highly imbalanced dataset dominated by the no-change class. Since labeling all

samples as "no change" yields high accuracy, we use the F1-score to emphasize precision and recall for the minority (change) class. This aligns with evaluation methods in sparse time series anomaly detection [32].

2) Standardized Mean Difference: Another way to evaluate ESST effectiveness is Standardized Mean Difference (SMD), which quantifies difference between two groups [33]. It is suitable for our telemetry, which vary in scale and units. We use Cohen's *D*, calculated with the pooled standard deviation; ± 0.2 indicates a small difference, while ± 0.8 or higher indicates a large difference.

3) MESST Score Variance: In MESST, variance measures dataset noise by averaging the squared differences from the mean. Evaluating variance over the entire signal is unhelpful, since the mean changes during faults. Instead, variance should be assessed separately for normal scores and fault spikes. This shows whether sensor fusion reduces noise in non-faulty data and amplifies spikes during faults. To do this, segment the score signal by time: a (start of drilling), b (fault onset), and c (fault end). For example, the variance of the nominal fault-free score can be calculated as:

$$\sigma^2_{[a,b]} = \frac{1}{b-a+1} \sum_{t=a}^{b} \left(x_t - \mu_{[a,b]}\right)^2 \tag{6}$$

with the goal to minimize the variance for the nominal fault free section and maximize the variance in our faulty section. For simplicity, we can define our nominal fault-free time sections as $\sigma_n = \sigma^2_{[a,b]}$ and our faulty sections $\sigma_f = \sigma^2_{[b,c]}$, where we want to minimize σ_n and maximize σ_f.

IV. Experiments

In general terms, faults tend to raise variables like motor torque τ and weight on bit ϕ while the rate of penetration ρ is roughly zero. The drill string auger velocity ω often has sudden dips from getting caught or stuck briefly with increased friction in the borehole preceding a fault.

For field testing in Haughton Crater, we monitored telemetry variables τ, ρ, ϕ, and their change scores S_τ, S_ρ, and S_ϕ. For the Antarctic fieldwork we measured τ, ρ, ϕ, and ω and their respective change S_τ, S_ϕ, S_ρ, S_ω, along with multivariate sensor fusion scores $S_{\tau,\omega}$ and $S_{\rho,\phi}$. From past field experience, faults must be detected quickly from symptom onset to enable mitigation, usually within 10-20 seconds from the symptom onset. Our experiments were designed to evaluate success within this tight time period.

A. Lab Testing Experiments

1) Implementation and Testing on Drill Hardware: ESST has been tested offline on the TRIDENT drill using recorded telemetry [28]. When integrating ESST with the drill avionics via PLEXIL at 40 Hz, we faced a trade-off between lower-rate sampling with data gaps and higher-rate sampling with potential duplicates. We chose lower-rate sampling and validated ESST with skipped time steps. As shown in Figure 3, the drill avionics pass motor telemetry to the PLEXIL Executive, which sends incremental data windows to the ESST/MESST Module. These windows are decomposed into both univariate and multivariate Hankel matrices, and the right singular vectors are used to detect significant changes and compute a score. The ESST and MESST scores are then passed to the user for evaluation. Testing before field deployment was done using composite materials designed to trigger faulty conditions with setup shown in Figure 2.

B. ESST Validation at Haughton Crater

1) Field Site Evaluation: The Haughton Impact Structure, a 23 km-wide crater on Devon Island, Nunavut, Canada, is a

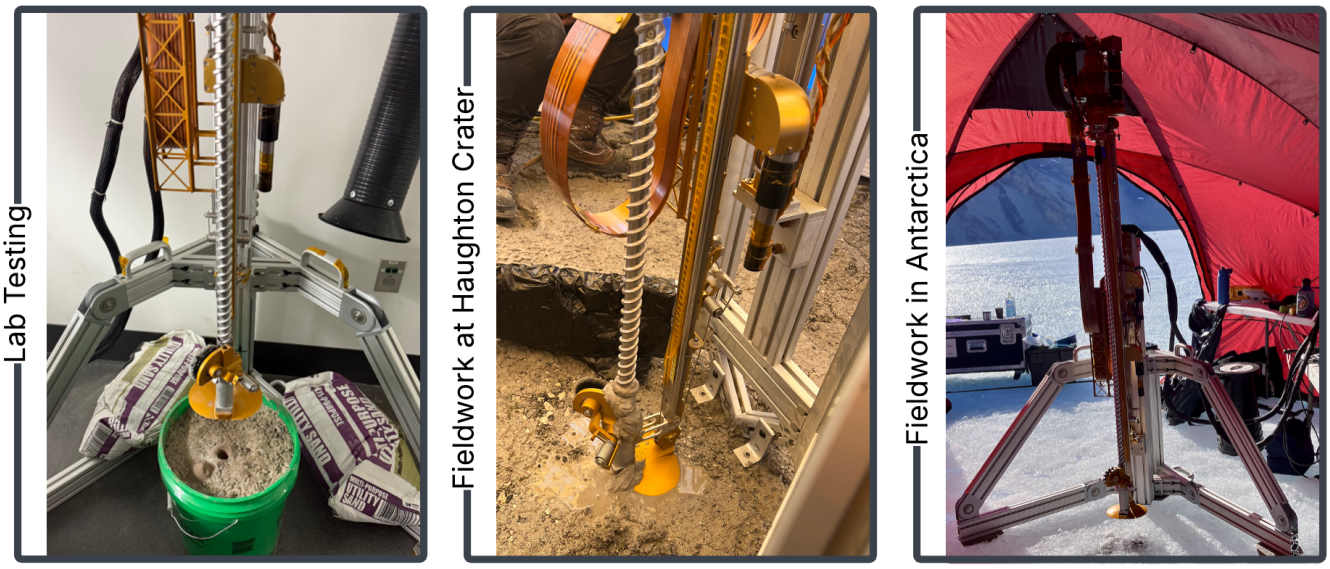

Fig. 2. Left: lab testing using regolith simulant buckets designed to quickly induce faults. Middle: drilling up to 1 m at Haughton Crater field site, validating ESST fault and anomaly detection software in an environment mimicking Mars conditions. Right: drilling up to 1 m at Lake Untersee, Antarctica, evaluating MESST Sensor Fusion in another planetary analog.

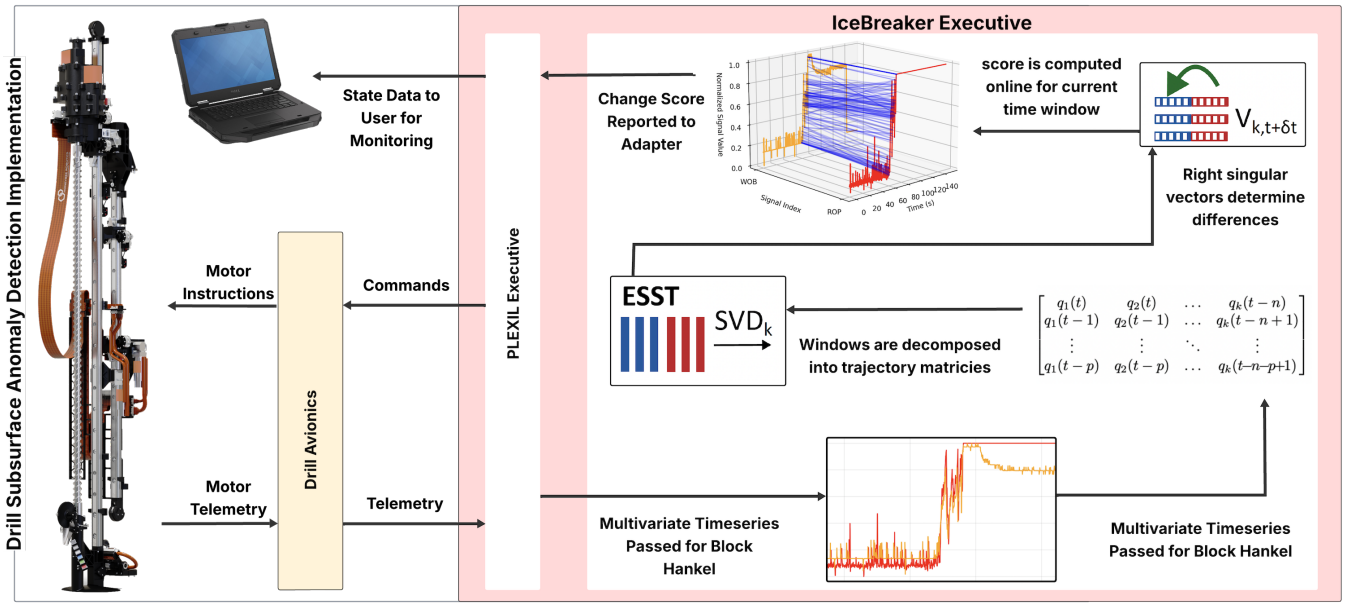

Fig. 3. Multivariate Subsurface Anomaly Detection Implementation. Motor Telemetry comes into the drill avionics. The telemetry is fed to the PLEXIL executive at a rate of 40Hz, and passes windows of data to our MESST Module. The data windows are then decomposed into block Hankel matrices and the right singular vectors determine any significant changes, which are then used to compute the multivariate score. The change score is then passed to the user.

well-studied Mars analog site [34]. Its cold, dry environment closely resemble Martian surface conditions and are thus ideal for testing space technologies. Features like frost polygonal terrain commonly seen in Martian high-latitude imagery make it ideal for surface and subsurface exploration research [35], [36], [37]. Haughton Crater has hosted previous Mars analog drilling tests [38] [39]. An interdisciplinary team selected likely sites for a Mars lander like in Figure 2.

C. MESST Validation in Antarctica

1) Field Site Evaluation and Testing Protocol: An interdisciplinary team selected drilling test sites with some characteristics similar to expectations for a Mars rover in the Antarctic in January 2026. Three locations in Schirmacher Oasis were chosen for their cold-desert ice-free Mars-analog location, with permafrost found at 20-30cm of depth and featuring geomorphic processes and microbial thermophiles. The long-term stable hard ice covering Lake Untersee was also a selected drilling test site. Aspects of both sites have been used as a Mars analog by other investigations [4], [5].

2) Experiments: Since past work has demonstrated the effectiveness of the ESST method for fault detection, we do not evaluate the fault detection capabilities of this method and instead focus on sensor fusion for noise control. This requires splitting our data into nominal sections σ_n and faulty section σ_f. We defined our nominal fault-free time sections and faulty sections in our methods. We want to minimize σ_n and maximize σ_f, evaluating our time segments using equation 6. For our experiments, we have fused signals S_τ (torque) and S_ω (auger velocity) to create $S_{\tau,\omega}$ and separately fused signals S_ρ (rate of penetration) and S_ϕ (weight on bit) to create $S_{\rho,\phi}$.

Ideally, fusing two noisy signals reduces variance in the nominal region. However, as shown in Figure 5, the signals often share trends but differ in noise levels, with some already low-noise, making it unrealistic for the fused signal to outperform both inputs. Instead, we target a fused signal with lower variance than at least the noisier input, with reduction relative to both inputs considered ideal. For faulty segments, the fused signal should exhibit higher variance than at least one input, ideally exceeding both to enhance fault sensitivity.

V. Results

A. Lab Testing Experiments

Lab tests allowed monitoring of drill and telemetry in a structured environment. We encountered six faults. Results appear in first row of Figure 4 and lab column of Table I. Upper right of Figure 4 shows torque (τ) and its change score. After percussion begins, the change score rises with τ due to increased cuttings or bit inclusion, often faulty if unaddressed. In this case, τ increased until a fault occurred.

1) SMD: After verifying timestamps, we labeled our timeseries data, checked our change scores from the ESST algorithm, which is plotted in 4. The change scores are noted in Table I. All our datasets had a Cohen's D score greater than $\pm$ 0.8, indicating the faulty telemetry data had a significant difference from the non-faulty telemetry data, giving us the ability to classify faulty and non-faulty telemetry and scores based on where it falls on our distribution.

2) F1 Score: For the F1-Score, in Table I, the closer to 1, the higher the precision and recall. We desire scores above 0.6. Numbers are rounded to two significant digits. Change scores of S_τ (torque) and S_ρ (weight on bit) all

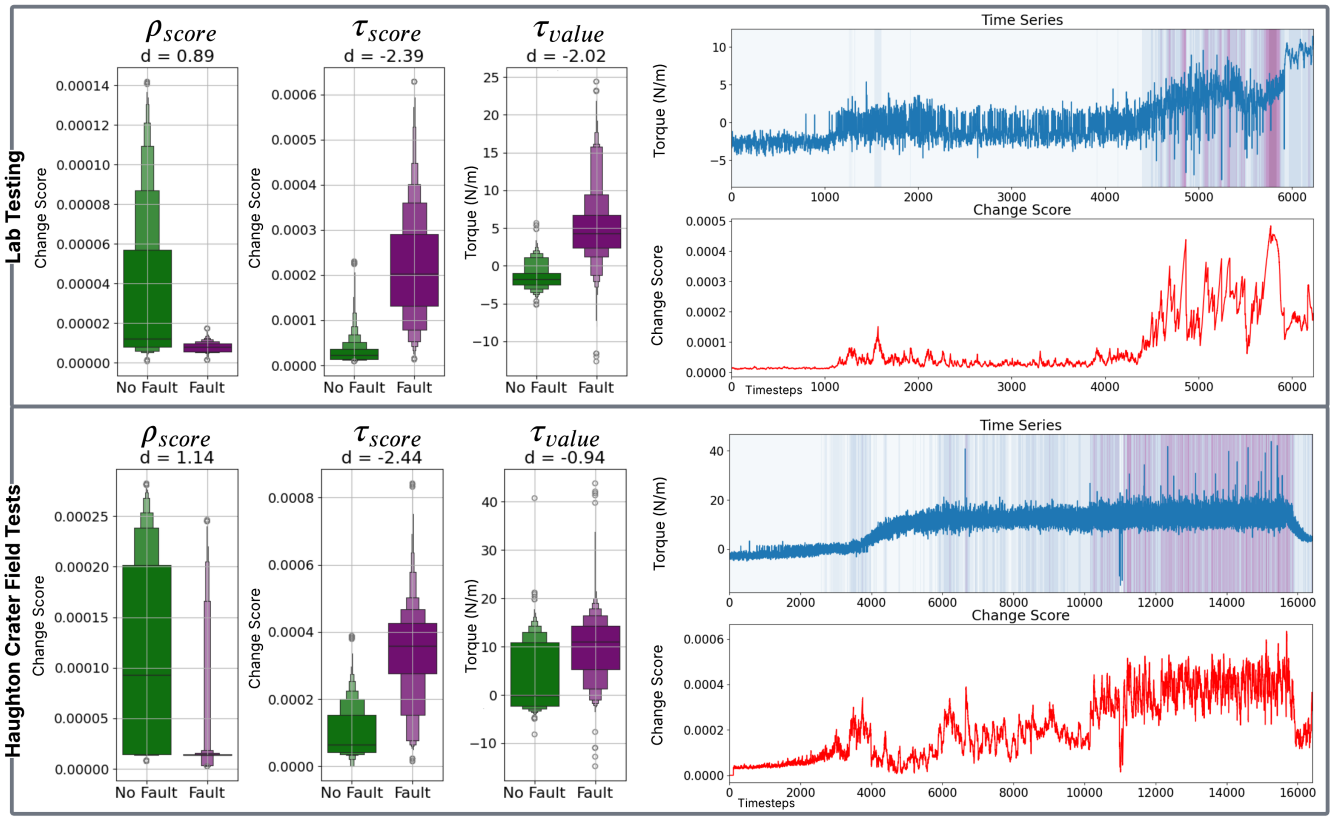

Fig. 4. Top: results from lab testing. Bottom: results from field testing. Left graphs in top and bottom show score distributions and Cohen's D score showing the difference between faulty and non-faulty datasets. Right graphs in top and bottom show motor torque τ time series data over a fault with the corresponding online change score. Purple shading indicates severity of the change score, with severity increasing with the buildup to the fault.

scored approximately above 0.6, indicating excellent true fault detection.

B. ESST Validation at Haughton Crater

We had five fault-free and three faulty drilling instances. Faults were identified offline using telemetry of τ and ρ, along with field notes on time, depth, and behavior. Field site results are shown in the second row of Figure 4. The lower right plot in Figure 4 shows a τ fault graph from the field, with progression similar to the lab example.

TABLE I
SMD COHEN'S D VALUE AND F1 SCORES FOR ALL RESULTS

Value	**Dataset Cohen's D Value**	
Location	**Lab**	**Field Site**
τ value	-2.02	-0.94
τ score	-2.39	-2.44
ρ score	0.89	1.14
Value	**Average F1 Score**	
Location	**Lab**	**Field Site**
τ score	0.82	0.75
ρ score	0.68	0.78

1) SMD: We calculated SMD scores as in the lab test. They are shown in Figure 4 and in Table I. All of our datasets had a Cohen's D score greater than ± 0.8, indicating faulty telemetry data for our datasets had a significant difference from our non-faulty telemetry data, reflecting lab results.

2) F1 Score: The F1-Scores are shown in Table I follow the same procedure as our lab experiments. For our field data, we evaluated the τ score and ρ score. All of our lab datasets scored above 0.6, indicating good true positive recall.

C. MESST Evaluation in Antarctica

We encountered 7 fault instances and evaluated variance of univariate ESST and multivariate MESST scores over the σ_n and σ_f segments, taking weighted averages across samples. Signals were first evaluated visually and against field notes and log files to judge fault onset and mark timestamps before evaluating ESST and MESST change scores. For the first sensor fusion evaluation, we examine $S_{\tau,\omega}$, S_τ, and S_ω in Table II. For σ_n, the sensor fusion helped significantly reduce

TABLE II
WEIGHTED AVERAGE VARIANCE FOR (σ_n) AND (σ_f) SEGMENTS

Signal	$\sigma^2(\sigma_n)$	$\sigma^2(\sigma_f)$
$S_{\tau,\omega}$	0.001378838	0.082164826
S_τ	0.006287162	0.046934778
S_ω	0.000000009	0.024155776
$S_{\rho,\phi}$	0.026078975	0.050281532
S_ρ	0.027251228	0.065119327
S_ϕ	0.019044157	0.025253024

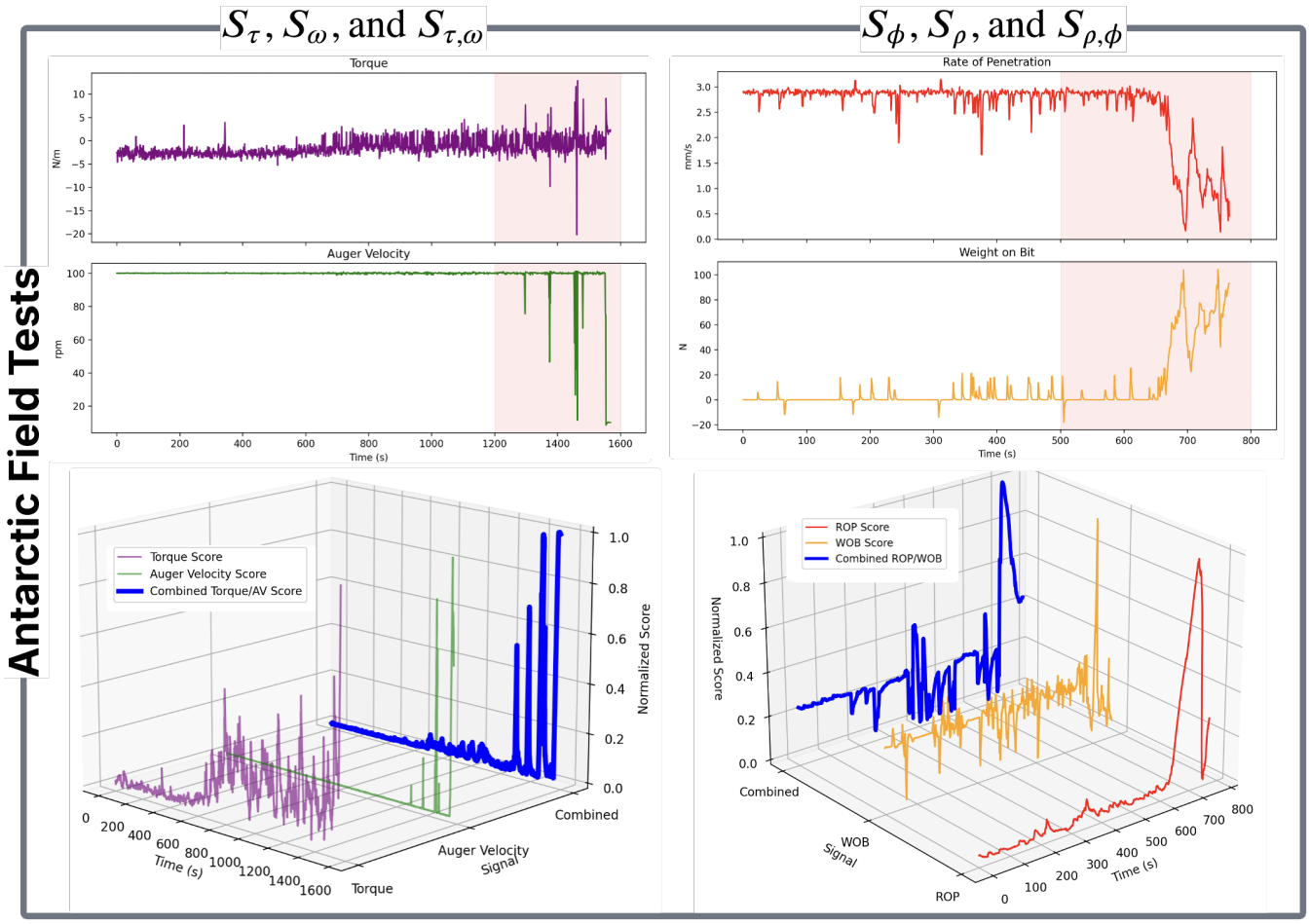

Fig. 5. Top left: torque τ, auger velocity ω signals. Top right: rate of penetration ρ and weight on bit ϕ. Bottom left: individual ESST change scores and fused MESST scores for torque and auger velocity. Bottom right: individual ESST change scores and fused MESST scores for rate of penetration and weight on bit.

the noise in S_τ, while slightly increasing the variance from S_ω. For σ_f, the variance of our $S_{\tau,\omega}$ increased significantly over the individual S_τ and S_ω signals, which means the sensor fusion significantly increased faulty variance. For the second sensor fusion evaluation, $S_{\rho,\phi}$, S_ρ, and S_ϕ, both signals had some noise in the σ_n grouping, with S_ρ being significantly more noisy than S_ϕ. However, overall $S_{\rho,\phi}$ did decrease compared to the most noisy signal. For our σ_f, the variance of our $S_{\rho,\phi}$ increased over the individual S_ϕ signals, increasing the faulty variance for one of the signals.

VI. Discussion

A. ESST

For the lab experiments, ESST reinforces prior findings [28], showing that online telemetry monitoring improves anomaly and fault detection despite limited data, supporting field deployment. For the Haughton Crater evaluation, results from ρ score, τ score, and τ telemetry indicate effective subsurface anomaly and fault detection.

B. MESST

For $S_{\tau,\omega}$, the sensor fusion reduced the noise in the S_τ signals significantly for our σ_n segments. It slightly increased variance in S_ω, but because the noise level for S_ω tends to be quite low (for example, 5 notes negligible noise increase with fault). For our σ_f segment, we found variance generally increased significantly in $S_{\tau,\omega}$ over both individual signals S_τ and S_ω. This is the best case for $S_{\tau,\omega}$. Similarly for $S_{\rho,\phi}$, the sensor fusion, $S_{\rho,\phi}$, reduced the noise in the S_ρ signal for our σ_n segments. For our σ_f segment, variance increased in $S_{\rho,\phi}$ over S_ϕ. MESST performed well in the field, reducing noise in $S_{\tau,\omega}$ and improving fault detection, while also lowering noise in $S_{\rho,\phi}$ without degrading performance.

VII. Conclusions and Future Work

This work evaluated ESST for univariate fault detection at Haughton Crater and introduced MESST, a multivariate method effective for signal stability and noise control for fault and anomaly detection methods, with a field evaluation in Antarctica. We validated ESST's continued effective fault and anomaly detection in the field, and found MESST reduced signal noise via sensor fusion fault and anomaly detection. Future work includes incorporating both these fault and anomaly detection methods into autonomous drilling models.

REFERENCES

[1] B. Glass, D. Bergman, V. Parro, L. Kobayashi, C. Stoker, R. Quinn, A. Davila, P. Willis, W. Brinckerhoff, K. Warren-Rhodes, M. Wilhelm, L. Caceres, J. DiRuggiero, K. Zacny, M. Moreno-Paz, A. Dave, S. Seitz, A. Grubisic, M. Castillo, R. Bonaccorsi, and the ARADS Team, "The Atacama rover astrobiology drilling studies (ARADS) project," *Astrobiology*, vol. 23, pp. 1245–1258, 2023.

[2] S. Boelter, G. Brown, L. Weber, T. Stucky, B. Glass, and M. Gini, "Model-free subsurface anomaly detection using subspace analysis techniques for sparse telemetry for extraterrestrial drilling robots," *Proc. IEEE Int'l Conf. on Robotics and Automation (ICRA), in press*, 2026.

[3] "Analog Missions - NASA — nasa.gov," https://www.nasa.gov/analog-missions/, [Accessed 12-09-2025].

[4] R. Hoover, "Schirmacher oasis/lake untersee antarctica astrobiology expedition expedition report flag 162," United States Space and Rocket Center, Tech. Rep., 05 2008.

[5] C. P. McKay, D. Andersen, and A. Davila, "Antarctic environments as models of planetary habitats: University Valley as a model for modern Mars and Lake Untersee as a model for Enceladus and ancient Mars," *The Polar Journal*, vol. 7, no. 2, pp. 303–318, 2017. [Online]. Available: https://doi.org/10.1080/2154896X.2017.1383705

[6] N. Muscettola, P. P. Nayak, B. Pell, and B. C. Williams, "Remote agent: to boldly go where no AI system has gone before," *Artificial Intelligence*, vol. 103, no. 1–2, pp. 5–47, 1998.

[7] G. Paulsen, K. Zacny, P. Chu, E. Mumm, K. Davis, S. Frader-Thompson, K. Petrich, D. Glaser, P. Bartlett, H. Cannon, and B. Glass, *Robotic Drill Systems for Planetary Exploration*. AIAA, 2006.

[8] P. W. Bartlett, D. Wettergreen, and W. R. L. Whittaker, "Design of the scarab rover for mobility and drilling in the lunar cold traps," in *Proceedings of the International Symposium on Artificial Intelligence, Robotics and Automation in Space (i-SAIRAS '08)*, 2008, pp. 3–6.

[9] J. Wei, A. Wang, J. L. Lambert, D. Wettergreen, N. Cabrol, K. Warren-Rhodes, and K. Zacny, "Autonomous soil analysis by the Mars Micro-beam Raman Spectrometer (MMRS) on-board a rover in the Atacama desert: a terrestrial test for planetary exploration," *Journal of Raman Spectroscopy*, vol. 46, no. 10, pp. 810–821, 2015. [Online]. Available: https://analyticalsciencejournals.onlinelibrary.wiley.com/doi/abs/10.1002/jrs.4656

[10] Y. Liu, Z. Yuan, Y. Li, and H. Zhao, "A Three-dimensional path planning method of autonomous burrowing robot for lunar subsurface exploration," in *2021 6th IEEE International Conference on Advanced Robotics and Mechatronics (ICARM)*, Jul. 2021, pp. 710–715. [Online]. Available: https://ieeexplore.ieee.org/document/9536059/

[11] H. Kolvenbach *et al.*, "Lunarleaper—a mission concept to explore the lunar subsurface with a small-scale legged robot," *Acta Astronautica*, vol. 240, pp. 63–75, 2026. [Online]. Available: https://www.sciencedirect.com/science/article/pii/S0094576525008082

[12] T. S. Vaquero *et al.*, "EELS: Autonomous snake-like robot with task and motion planning capabilities for ice world exploration," *Science Robotics*, vol. 9, no. 88, p. eadh8332, Mar. 2024. [Online]. Available: https://www.science.org/doi/full/10.1126/scirobotics.adh8332

[13] L. Balzano, Y. Chi, and Y. Lu, "Streaming PCA and subspace tracking: The missing data case," *Proceedings of the IEEE*, vol. PP, 2018.

[14] L. Balzano, R. Nowak, and B. Recht, "Online identification and tracking of subspaces from highly incomplete information," in *2010 48th Annual Allerton Conference on Communication, Control, and Computing (Allerton)*, 2010, pp. 704–711.

[15] Y. Chi, Y. C. Eldar, and R. Calderbank, "PETRELS: Parallel subspace estimation and tracking by recursive least squares from partial observations," *IEEE Transactions on Signal Processing*, vol. 61, no. 23, pp. 5947–5959, 2013.

[16] T. Idé and K. Tsuda, "Change-point detection using Krylov subspace learning," in *Proceedings of the SIAM International Conference on Data Mining*, 2007, pp. 515–520.

[17] V. Moskvina and A. Zhigljavsky, "An algorithm based on singular spectrum analysis for change-point detection," *Communications in Statistics-Simulation and Computation*, vol. 32, no. 2, 2003.

[18] L. Weber and R. Lenz, "Accelerating singular spectrum transformation for scalable change point detection," *IEEE Access*, vol. 13, pp. 213 556–213 577, 2025.

[19] ——, "Machine learning in sensor identification for industrial systems," *it - Information Technology*, vol. 65, pp. 213 556–213 577, 2023.

[20] F. Deng, Y. Huang, S. Lu, Y. Chen, J. Chen, H. Feng, J. Zhang, Y. Yang, J. Hu, T. L. Lam, and F. Xia, "A multi-sensor data fusion system for laser welding process monitoring," *IEEE Access*, vol. 8, pp. 147 349–147 357, 2020.

[21] Z. Huang, G. Ye, P. Yang, and W. Yu, "Application of multi-sensor fusion localization algorithm based on recurrent neural networks," *Scientific Reports*, vol. 15, no. 1, p. 8195, 2025. [Online]. Available: https://doi.org/10.1038/s41598-025-90492-4

[22] S. Yao, S. Hu, Y. Zhao, A. Zhang, and T. Abdelzaher, "Deepsense: A unified deep learning framework for time-series mobile sensing data processing," in *Proc. 26th Int'l Conference on World Wide Web*, ser. WWW '17. Geneva, CH: International World Wide Web Conferences Steering Committee, 2017, p. 351–360. [Online]. Available: https://doi.org/10.1145/3038912.3052577

[23] P. Frame and A. Towne, "Space-time POD and the Hankel matrix," *PLOS ONE*, vol. 18, no. 8, pp. 1–31, 08 2023. [Online]. Available: https://doi.org/10.1371/journal.pone.0289637

[24] D. Zhang, J. He, Y. Zhou, D. Chen, and Z. Wang, "Hybrid low-rank and sparsity constraint with hankel structure preservation for simultaneous seismic reconstruction and denoising," *IEEE Geoscience and Remote Sensing Letters*, vol. 20, pp. 1–5, 2023.

[25] W. Sun, Y. Zhou, J. Xiang, B. Chen, and W. Feng, "Hankel matrix-based condition monitoring of rolling element bearings: An enhanced framework for time-series analysis," *IEEE Transactions on Instrumentation and Measurement*, vol. 70, pp. 1–10, 2021.

[26] F. Golnary, H. Kalhori, B. Li, and B. Halkon, "Hankel matrix denoising for enhanced subspace state–space system identification in modal analysis," *Mechanical Systems and Signal Processing*, vol. 246, p. 113843, 2026. [Online]. Available: https://www.sciencedirect.com/science/article/pii/S0888327025015444

[27] Y. Zhang, M. Yu, Y. Wang, and C. Han, "A rubbing fault identification method of combining the covariance of the Hankel matrix and 1D-LBP," *Structural Health Monitoring*, vol. 0, no. 0, p. 14759217251340663, 2025. [Online]. Available: https://doi.org/10.1177/14759217251340663

[28] S. Boelter, L. Weber, R. Lenz, B. Glass, and M. Gini, "Fault prediction in drilling using subspace analysis techniques," *Intelligent Autonomous Systems 19, Proc. 19th Int'l Conf IAS-19*, 2025.

[29] G. J. J. van den Burg and C. K. I. Williams, "An evaluation of change point detection algorithms," arXiv:2003.06222v3 [stat.ML], 2020.

[30] S. Aminikhanghahi and D. J. Cook, "A survey of methods for time series change point detection," *Knowl. Inf. Syst.*, vol. 51, no. 2, p. 339–367, 2017.

[31] C. Truong, L. Oudre, and N. Vayatis, "Selective review of offline change point detection methods," *Signal Processing*, vol. 167, no. C, 2020.

[32] S. Schmidl, P. Wenig, and T. Papenbrock, "Anomaly detection in time series: A comprehensive evaluation," *Proceedings of VLDB Endowment*, vol. 15, no. 9, pp. 1779–1797, 2022.

[33] C. Andrade, "Mean difference, standardized mean difference (smd), and their use in meta-analysis: As simple as it gets," *The Journal of Clinical Psychiatry*, vol. 81, no. 5, p. 11349, 2020.

[34] G. R. Osinski, P. Lee, J. G. Spray, J. Parnell, D. S. S. Lim, T. E. Bunch, C. S. Cockell, and B. Glass, "Geological overview and cratering model for the Haughton impact structure, Devon Island, Canadian High Arctic," *Meteoritics & Planetary Science*, vol. 40, no. 12, pp. 1759–1776, 2005.

[35] T. D. Barfoot, P. T. Furgale, B. E. Stenning, P. J. F. Carle, J. P. Enright, and P. Lee, "Devon island as a proving ground for planetary rovers," in *Brain, Body and Machine*, J. Angeles, B. Boulet, J. J. Clark, J. Kövecses, and K. Siddiqi, Eds. Berlin, Heidelberg: Springer Berlin Heidelberg, 2010, pp. 269–281.

[36] P. Furgale, P. Carle, J. Enright, and T. D. Barfoot, "The Devon Island rover navigation dataset," *The International Journal of Robotics Research*, vol. 31, no. 6, pp. 707–713, May 2012. [Online]. Available: https://journals.sagepub.com/doi/10.1177/0278364911433135

[37] T. D. Barfoot, P. T. Furgale, G. R. Osinski, N. Ghafoor, and K. K. Williams, "Field testing of robotic technologies to support ground ice prospecting in martian polygonal terrain," *Planetary and Space Science*, vol. 58, no. 4, pp. 671–681, Mar. 2010. [Online]. Available: https://linkinghub.elsevier.com/retrieve/pii/S0032063309002852

[38] B. Glass, H. Cannon, M. Branson, S. Hanagud, and G. Paulsen, "DAME: Planetary-prototype drilling automation," *Astrobiology*, vol. 8, pp. 653–64, 2008.

[39] B. J. Glass, A. Dave, C. P. McKay, and G. Paulsen, "Robotics and automation for "Icebreaker"," *Journal of Field Robotics*, vol. 31, no. 1, pp. 192–205, Jan. 2014. [Online]. Available: https://onlinelibrary.wiley.com/doi/10.1002/rob.21487